

Time-Resolved Film-Cooling Flows at High and Low Density Ratios

Molly K. Eberly

Applied Research Laboratory,
The Pennsylvania State University,
State College, PA 16804
e-mail: mke5007@psu.edu

Karen A. Thole

Mechanical and Nuclear Engineering Department,
The Pennsylvania State University,
University Park, PA 16802
kthole@enr.psu.edu

Film-cooling is one of the most prevalent cooling technologies that is used for gas turbine airfoil surfaces. Numerous studies have been conducted to give the cooling effectiveness over ranges of velocity, density, mass flux, and momentum flux ratios. Few studies have reported flowfield measurements with even fewer of those providing time-resolved flowfields. This paper provides time-averaged and time-resolved particle image velocimetry data for a film-cooling flow at low and high density ratios. A generic film-cooling hole geometry with wide lateral spacing was used for this study, which was a 30 deg inclined round hole injecting along a flat plate with lateral spacing $P/D=6.7$. The jet Reynolds number for flowfield testing varied from 2500 to 7000. The data indicate differences in the flowfield and turbulence characteristics for the same momentum flux ratios at the two density ratios. The time-resolved data indicate Kelvin–Helmholtz breakdown in the jet-to-freestream shear layer. [DOI: 10.1115/1.4025574]

1 Introduction

Gas turbine engines are widely used in the power generation and aircraft propulsion industries. With rising fuel costs and an increased awareness of the effects of carbon emissions on the environment, it has become increasingly important that jet engines operate as efficiently as possible. The turbine hardware is cooled because the combustion gases reach temperatures higher than the turbine material's melting temperature, which significantly reduces the part's lifespan. Increasing the turbine pressure ratio increases the efficiency of the engine, but also increases the need for engine cooling techniques. Unfortunately, the use of compressor bleed air for cooling acts as a parasitic drain on the engine and lowers the overall engine efficiency, taking valuable air from the compressor and using it as coolant instead of for powering the engine. For this reason, engine developers want to use this coolant air as efficiently as possible.

Film-cooling is a method by which compressor bleed air is directed through a series of discrete holes onto the surface of turbine engine components to cool and protect the surface from hot engine gases. Many different physical parameters define film-cooling effectiveness. These parameters can be unique to the film-cooling geometry, such as the hole length, hole angle, lateral hole spacing, and hole shape. This study will address cylindrical holes oriented axially with a wide lateral spacing. In addition, defining parameters can be directly related to a series of ratios between the coolant and freestream gas flow. These flow characteristics include density ratio (DR), momentum flux ratio (I), blowing (mass flux) ratio (M), and velocity ratio (VR).

A new facility was developed to conduct flat plate film-cooling studies at high density ratios. Density ratio in a turbine engine is typically between 1.5 and 2.0. The facility uses cryogenic cooling to achieve high density ratio, based on the facility described in Pietrzyk et al. [1]. The facility was benchmarked and used for making the flowfield measurements reported in this paper.

2 Previous Studies

Many studies have been conducted to further understand the parameters that influence film-cooling. While an exhaustive list of film-cooling studies will not be reported in this paper, it is

important to cite papers that have shown the effect of density ratio. Schmidt et al. [2] performed high density ratio film-cooling studies for a flat plate and Wayne and Bogard [3] studied the suction side of an airfoil. Schmidt et al. [2] and Wayne and Bogard [3] found that higher density ratios contributed to a higher film-cooling effectiveness than lower density ratios, and the effects of density ratio were apparent for high blowing ratio cases while comparatively smaller for low blowing ratios. They also studied the effect of lateral hole spacing on film-cooling effectiveness, and found that the laterally averaged effectiveness scaled linearly with the distance between holes [2,3].

Fewer flowfield measurements have been conducted to better understand the physics of the flow that governs film-cooling effectiveness. Pietrzyk et al. [1,4] used laser-Doppler velocimetry (LDV) to study the flowfield for a cylindrical hole at both unit density ratio and high density ratio. They postulated the existence of a separation region inside the film-cooling hole that caused turbulence peaks at the upstream and downstream edges of the hole. They also found that the turbulence intensity scaled with velocity ratio.

Fric and Roshko [5] identified four dominant fluid structures present in a film-cooling jet in crossflow: shear layer vortices, horseshoe vortices, counter-rotating vortex pair (CRVP), and wake vortices. Their study focused on the wake vortices, and found that the wake vortices originate at the boundary layer and attach to the jet periodically. The CRVP has been a widely studied structure in film-cooling, because it seriously affects film-cooling performance. Haven and Kurosaka [6] measured the presence of both kidney (CRVP) and antikidney vortices present in a shear layer of a jet in crossflow injected at 90 deg.

One of the more recently used techniques in measuring flowfields is particle image velocimetry (PIV), which is desirable because of its ability to capture a two-dimensional spatial map. Kampe et al. [7] utilized PIV to study the effects of a diffused hole shape as compared to a cylindrical hole. The diffused hole jet was no longer dominated by the familiar CRVP, but was instead dominated by a lateral spreading of the jet. Three flowfield components can be measured with the use of two cameras, as was used by Bernsdorf et al. [8]. They also measured the characteristic CRVP at varying density ratios and blowing ratios. The axial component of the CRVP increased with increasing blowing ratio and the center of the CRVP was closer to the wall at higher density ratios.

More recently, methods for capturing time-resolved flowfield data have been developed. Tanahashi et al. [9] developed a

Contributed by the International Gas Turbine Institute (IGTI) of ASME for publication in the JOURNAL OF TURBOMACHINERY. Manuscript received July 2, 2013; final manuscript received July 21, 2013; published online November 8, 2013. Editor: Ronald Bunker.

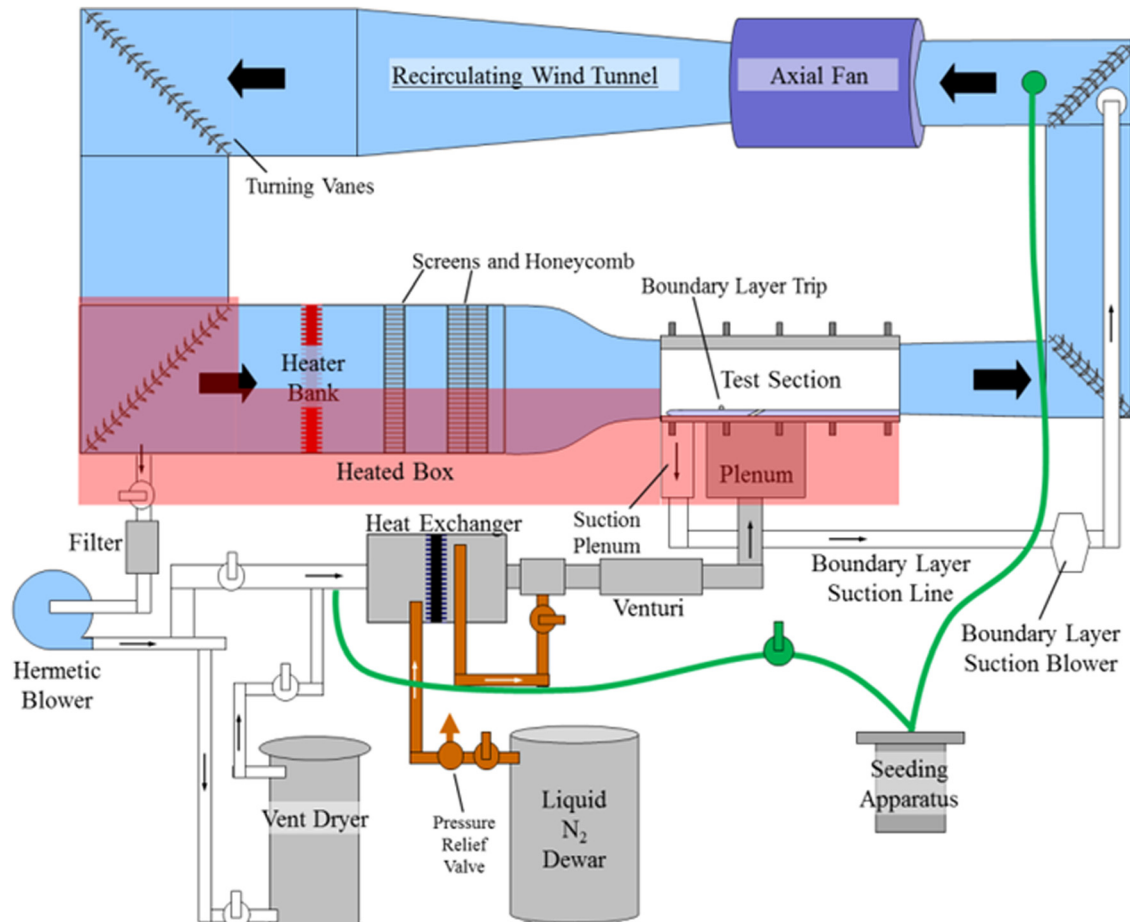


Fig. 1 Schematic of the flowfield and heat transfer facility with the nitrogen cooling system

method for stereoscopic, time-resolved PIV and showed that the experimental measurements are of the same ability to resolve small-scale eddies as direct numerical simulation. Time-resolved flow visualization was utilized by Fawcett et al. [10] at unit density ratio, which identified unsteady flow structures in the shear layer vortices of a film-cooling flow.

Numerous adiabatic effectiveness studies have been conducted, but fewer have been done with flowfield measurements. An understanding of the unsteady flow structures in film-cooling flows help to improve ways in which new turbulence models can be developed. Without time-resolved measurements, it is not possible to compare with large eddy simulations; for example. As computational models and resources increase, the gas turbine community will require unsteady data for benchmarking. To the best of the author's knowledge, there have been no time-resolved studies conducted at high density ratio on realistic film-cooling geometries. Most of the studies conducted in the past have been done with close hole spacings such as $P/D = 3$ and at low density ratios. This is the first paper from a new facility in which time-resolved flowfield measurements are reported for wide hole spacings at $P/D = 6.7$ for both high and low density ratios. In addition, this paper presents benchmarking for a new high density ratio test facility.

3 Experimental Facilities

Flowfield and adiabatic effectiveness measurements were made in the closed-loop wind tunnel facility shown in Fig. 1. The mainstream flow was driven by a 1.1 kW axial fan, which could supply mainstream velocities up to 16 m/s in the test section. The mainstream temperature was heated with a 1.4 kW heating bank and

cooled with a chilled-water circuit to maintain a constant temperature in the test section.

Optical access was achieved through acrylic side walls and a removable ceiling piece. The interchangeable ceiling contained a frame that could be installed with either a window made of Zinc Selenide (ZnSe) for the infrared camera measurements or glass for the time-resolved PIV measurements. Boundary layer suction was implemented just upstream of the test section to restart the boundary layer. A boundary layer trip upstream of the film-cooling holes ensured a turbulent incoming boundary layer. The boundary layer trip was $33D$ upstream of the film-cooling holes for all flowfield and boundary layer measurements and $14D$ upstream of the film-cooling holes for the adiabatic effectiveness measurements. Repeatability tests were conducted to ensure that the trip location did not affect the effectiveness results.

To ensure an adiabatic test plate, a heated box was added below the tunnel in which the heated mainstream temperature was matched, as shown by the shaded red region in Fig. 1. Several heaters were placed in the heated box that were controlled to match the mainstream temperature so no heat was lost through the bottom tunnel wall.

Air for the coolant loop was extracted directly from the wind tunnel mainstream flow, as shown in Fig. 1. This coolant air was driven by a hermetically-sealed 60 Hz variable frequency blower. The coolant air was then diverted through a vent dryer filled with solid desiccant, which removed moisture from the air. Once the air in the tunnel was sufficiently dried, the coolant flow traveled through a heat exchanger where it was cooled with liquid nitrogen. After the heat exchanger, the then-gaseous nitrogen was combined with the coolant flow directly to further cool the coolant. The flow then passed through a Venturi meter where the flow rate

Table 1 Parameters for film-cooling geometry

Geometry	D (mm)	L/D	P/D	α (deg)	# holes
Benchmarking	9.5	4.7	3	35	7
Axial cylindrical	8.2	4.7	6.7	30	5

was measured, after which it passed through a plenum and exited out the film-cooling holes. Coolant flow was fed to the film-cooling holes through a plenum with a pipe-to-plenum area ratio of 24. A splash plate and a porous plate inside the plenum ensured that the air was evenly distributed before entering the cooling holes. The coolant temperature was measured as the average of five thermocouples in the plenum near the film-cooling hole entrances.

Adiabatic effectiveness and flowfield experiments were conducted using the flat plate geometries listed in Table 1 and shown in Fig. 2. Benchmarking tests had a different geometry than the primary tests to match that found in the literature. Blowing ratios ranging from $M = 0.25$ to $M = 2.0$ were tested at both low density ratio and high density ratio. Low density ratio tests were conducted at $DR = 1.2$ and high density ratio tests were conducted at $DR = 1.6$. For adiabatic effectiveness studies the plate was manufactured from Dow STYROFOAM™ brand residential sheathing ($k = 0.029$ W/mK), while for flowfield studies the plate was manufactured out of medium density fiberboard to ensure the laser did not melt the test plate.

3.1 Adiabatic Effectiveness Measurements. The adiabatic effectiveness measurements were taken with an SC620 FLIR Infrared (IR) Camera. The camera had an operational range of -40°C to 120°C , with an accuracy of $\pm 2\%$ of the reading. The camera output images that were 480×640 pixels with an average resolution of 2.25 measurement pixels/mm, giving a measurement volume of $0.055D$ for this geometry. The IR camera was positioned so that it viewed the plate surface from above through a ZnSe window at the top of the test section.

To ensure steady-state conditions, all IR camera measurements were gathered three hours after the test conditions had been set. Five steady-state images were averaged together to create the 2-dimensional effectiveness contours shown in the results. Laterally-averaged data are presented as the average across three

hole pitches. The centerline data shown in the plots were also averaged for the center of the same three film-cooling holes. Because the experimental conditions for high density ratio exceeded the camera's output temperature range, a unique calibration method was implemented based on the one outlined in Polanka [11]. To begin a calibration, a test was set up so that simultaneous IR data and thermocouple data could be gathered. During that test, the mainstream conditions were kept constant while the coolant conditions were varied, so that an entire temperature range could be calibrated. The IR data was then matched with the thermocouple data for the thermocouple locations at each temperature and time step creating calibration curves. The equation of each curve was used to match each IR camera output image to a true temperature value for the entire plate to within $T = \pm 1.5^\circ\text{C}$ for high density ratio and $T = \pm 0.63^\circ\text{C}$ for low density ratio. More details about the calibration methods for this facility are given in Eberly [12].

3.2 Flowfield Measurements. Flowfield measurements were taken using LDV and time-resolved digital particle image velocimetry (TRDPIV). The flow was seeded with liquid atomized diethyl-hexyl-sebecat (DEHS). The DEHS particles were atomized to droplets with an average diameter of $1\ \mu\text{m}$ with a Stokes number of $St = 0.003$. The seeding particles were added to the flow in two locations: the mainstream just upstream of the tunnel fan and the coolant flow just downstream of the heat exchanger as shown in Fig. 1.

The boundary layer was measured using a single-component LDV and the TRDPIV. For the LDV, a beam separator split each component beam into a beam pair with one member of the pair being shifted by 40 Hz. Fiber optic probes with a 750 mm focusing lens produced an elliptical measurement volume that was $850 \times 72\ \mu\text{m}$ in major and minor diameter. Each data point was taken as an average of at least 10,000 instantaneous measurements over a span of more than eight seconds for each location. The LDV was set up to take boundary layer measurements at $x/D = -5.1$ through the acrylic side window.

Time-resolved flowfield measurements were gathered through TRDPIV. The laser sheet was sent through a glass window on the top of the test section. The TRDPIV experimental setup gathered data in a two-dimensional plane from $x/D = -5.5$ to $x/D = 8.0$ at two lateral locations shown in Fig. 2. One measurement plane was

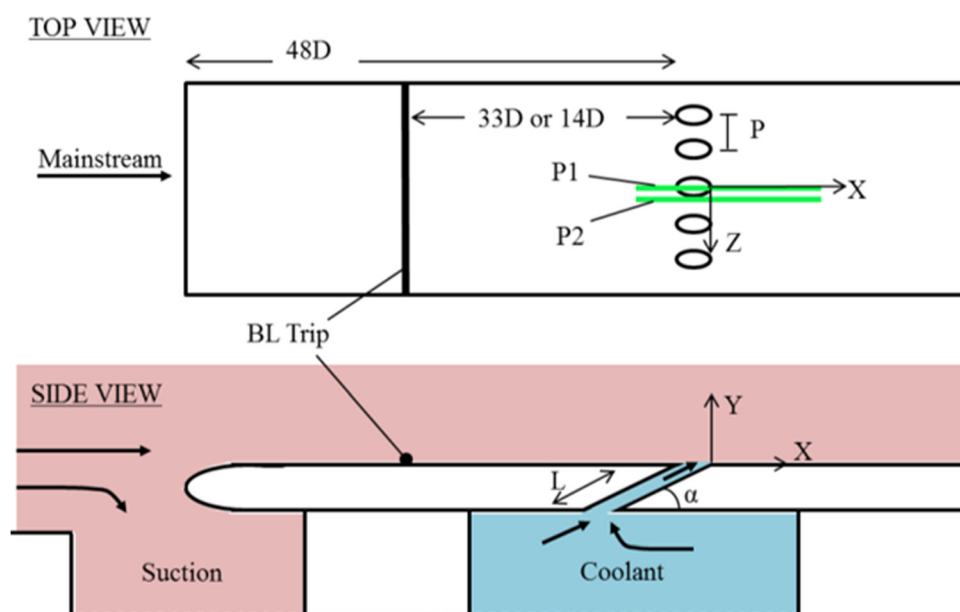


Fig. 2 Flat plate geometry for film-cooling studies

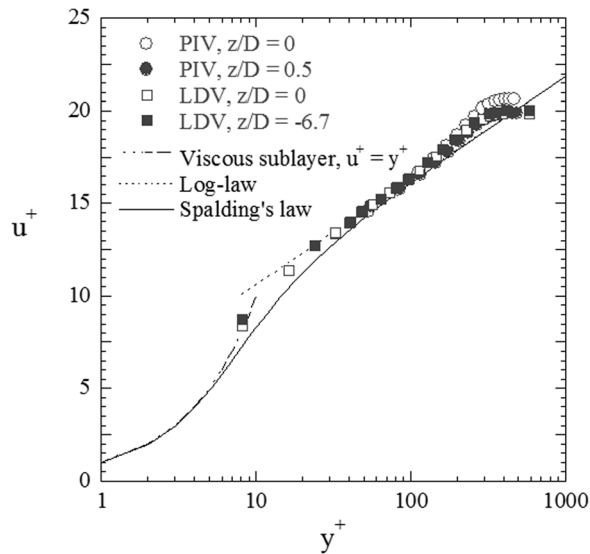


Fig. 3 Turbulent boundary layer profile in near-wall coordinates at $x/D = -5.1$, measured with LDV and TRDPIV

located at the centerline of the center of five holes (P1), and the second measurement plane was taken tangent to the lateral edge of the cooling hole (P2), at $z/D = 0.5$. Because of physical constraints in the test facility, only the x - y plane was studied. A 15 W Nd:YLF laser with a 10 kHz firing capability illuminated the seeding particles. A 2 kHz CMOS high speed camera placed normal to the laser sheet took pairs of images of the illuminated seed particles. The time delay between laser pulses was chosen based on the bulk movement of the fluid flow, and it was ensured that average bulk movement was less than 16 pixels, or $1/4$ the initial interrogation window size. Images were taken at 2 kHz with an image size of 1024×512 pixels and an image resolution of 8.3 pixels/mm. Time-averaged flowfield results were taken as the average of 6000 image pairs over a span of three seconds.

TRDPIV data was processed using LaVision's DaVis commercial software [13]. An average background image was subtracted to decrease signal-to-noise ratio. The images were processed using variable interrogation windows (decreasing size); with a first pass window size of 64×64 pixels with 50% overlap, a second pass window size of 32×32 pixels, and third and fourth pass window sizes of 16×16 pixels with 50% overlap. A cross correlation calculated the displacement vectors between pairs of images. Post-processing vector validation was performed in order to remove and replace spurious vectors, and in each case the validation was checked to make sure that important vectors were not removed. The postprocessing vector validation involved identifying spurious vectors, removing them, and then replacing them. A vector was defined as spurious if it was outside of the median of the surrounding vectors within a calculated average deviation.

4 Uncertainty Analysis

Uncertainty calculations were performed for the flat plate effectiveness studies as well as for the boundary layer LDV studies and the TRDPIV studies. A 95% confidence level was used for all uncertainty measurements. Uncertainty in density ratio and adiabatic effectiveness was found using the propagation of error method described in Figliola and Beasley [14] and Moffat [15]. Error for adiabatic effectiveness was dominated by the bias error of the thermocouples and the scatter of the calibration, and takes the value $\eta = \pm 0.025$ at high density ratio and $\eta = \pm 0.014$ at low density ratio. Uncertainty in density ratio was also dominated by the bias error of the thermocouples and was found to be $DR = \pm 0.3\%$ for both high and low density ratio. Uncertainty in

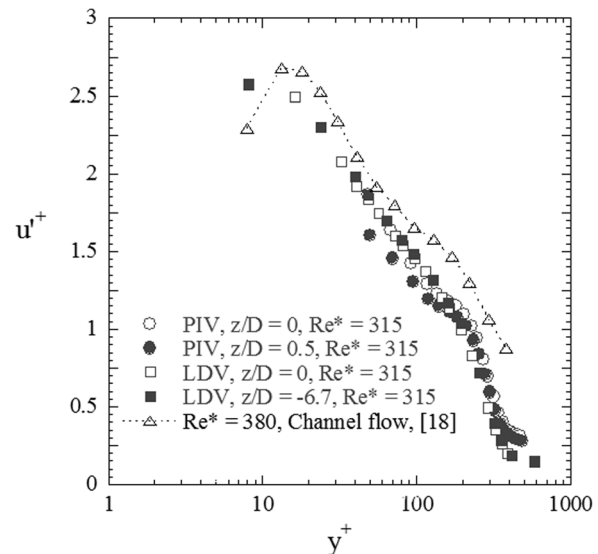


Fig. 4 Turbulent velocity fluctuations in near-wall coordinates at $x/D = -5.1$, measured with LDV and TRDPIV

Table 2 Boundary layer characteristics

θ/D	δ/D	Re_θ	Re^*	u^*
0.13	1.2	670	315	0.51 m/s

blowing ratio and velocity ratio was found to be 4% at $M = 2$, and uncertainty in momentum flux ratio was 8% at $I = 2.4$.

Precision uncertainty was assumed to be negligible for the TRDPIV measurements, since the data sets were so large that they achieved statistical convergence. Instead, uncertainty was calculated with respect to the maximum particle displacement gradient. For a given instantaneous data set, the maximum displacement gradients were $(\partial \bar{U} / \partial y)_{\max} = 0.45 px/px$, and $(\partial \bar{V} / \partial x)_{\max} = 0.24 px/px$. Using the uncertainty calculation process outlined in Raffel et al. [16] and Scarano and Riethmuller [17], the error in pixel displacement was approximated to be $\epsilon_u = 0.6 px$ and $\epsilon_v = 0.08 px$. The total uncertainty in local velocity measurements with TRDPIV was then calculated to be 4% for \bar{U} and 3.1% for \bar{V} .

5 Validation of Test Facility and Methods

The incoming flow velocity was spatially uniform to within 0.5% and the average turbulence intensity in the test section was 0.7%. A more detailed description of the flowfield benchmarking can be found in Eberly [12]. Boundary layer profiles were measured for the boundary layer trip position 33D upstream the film-cooling holes at $x/D = -5.1$ with both LDV and TRDPIV. Figure 3 and Fig. 4 give the near-wall boundary layer measurements with the LDV and TRDPIV. The boundary layer measurements are in agreement with near-wall log-law, Spalding's law, and viscous sublayer trends, as well as experimental data from Harder and Tiederman [18]. A summary of all the boundary layer results is given in Table 2. Friction velocity, u^* , was found experimentally from the boundary layer measurements, and can alternately be found using a correlation for skin friction coefficients, as provided in the nomenclature section.

Additionally, TRDPIV measurements were taken for a baseline test at $DR = 1$ and $M = 1$, as shown in Figs. 5 and 6. Previous LDV data had been taken by Thole et al. [19] and Pietrzyk et al. [1] three hole diameters downstream of the film-cooling hole at the same conditions. The streamwise velocity and fluctuating

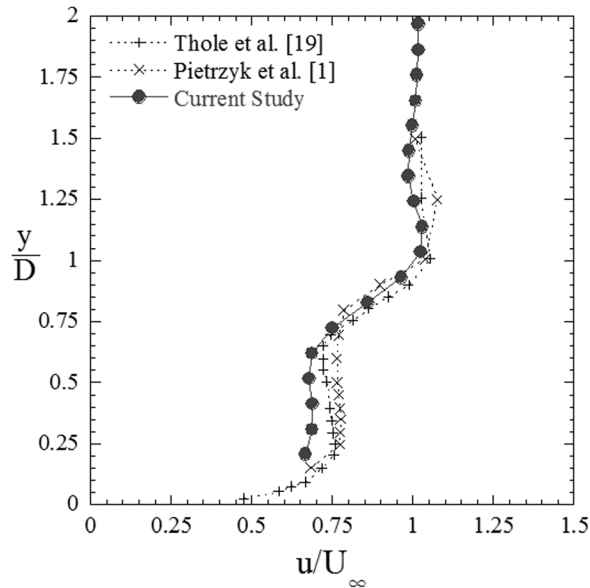


Fig. 5 Streamwise profile at $x/D = 3.0$ and the hole centerline location for film-cooling at, $M = 1.0$, and $DR = 1.0$

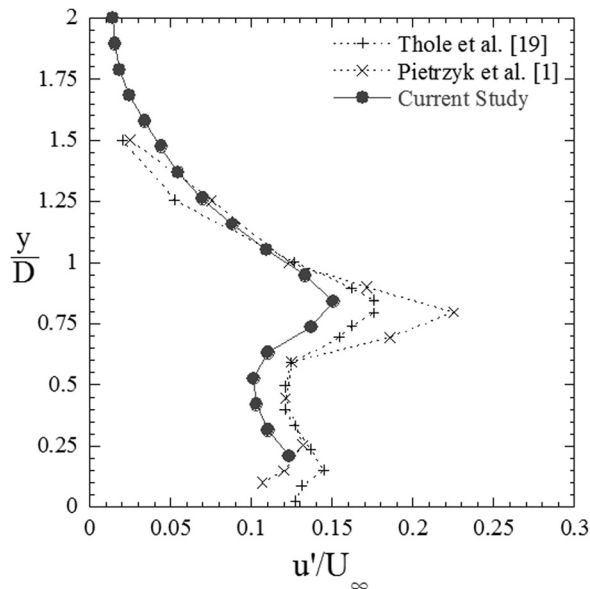


Fig. 6 Streamwise turbulent velocity fluctuations at $x/D = 3.0$ and the hole center location, $M = 1.0$, and $DR = 1.0$

velocity profiles at this location are in excellent agreement with the previous two studies. The agreement of the current study's TRDPIV streamwise velocity and turbulent velocity fluctuation profiles with the results of the studies done by [19] and [1] validates the film-cooling flowfield measurements.

To benchmark the test facility for adiabatic effectiveness measurements, geometric parameters were chosen to be similar to previously published data for an axial cylindrical hole, shown in Table 1. The benchmarking was performed with this geometry at high density ratio for blowing ratios of $M = 0.5$ and $M = 1$. High density ratio adiabatic effectiveness contours for the benchmarking geometry are shown in Fig. 7. The contours show good periodicity. Overall, the cooling jets have equivalent spreading, shape, and travel the same distance downstream. This periodicity shows that every hole receives equivalent cooling and adds confidence in the experimental setup.

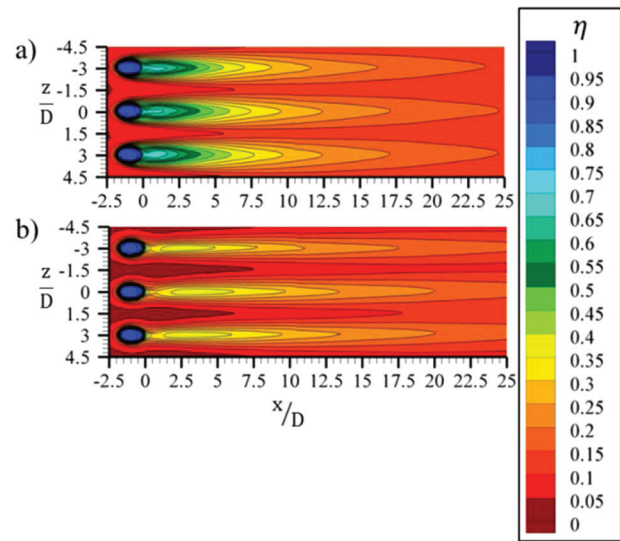


Fig. 7 High density ratio contours for closely-spaced axial cylindrical holes at blowing ratios (a) $M = 0.5$, $DR = 1.6$ ($I = 0.16$, $VR = 0.32$) and (b) $M = 1$, $DR = 1.6$ ($I = 0.61$, $VR = 0.61$)

Table 3 Previous studies at high density ratios

Study	P/D	L/D	α (deg)	DR	M	I
Current study	3	4.7	35	1.6	0.5	0.16
[20]	3	6	30	1.5	0.5	0.17
[21]	—	6	30	1.9	0.62	0.21
[22]	3	2.8	35	1.6	0.5	0.16
[2]	3	4	35	1.6	0.63	0.23
[23]	3	1.8	35	1.6	0.57	0.20
[24]	3	40	35	1.5	0.52	0.17

Table 3 gives a summary of studies reported in the literature to which the current benchmarking study is compared. The laterally averaged effectiveness plots for high density ratio are shown in Fig. 8. The injection angle and density ratio variation contribute to slight differences in the data. Overall, the results for high density ratio in the current study agree fairly well with those done in literature, giving confidence in the new facility, IR thermography measurements, and IR calibration techniques.

6 Effectiveness Results for $P/D = 6.7$

Flat plate film-cooling effectiveness experiments were conducted on a cylindrical geometry with widely-spaced holes to match the flowfield measurements. The geometry was as shown in Fig. 2 and Table 1, with lateral spacing $P/D = 6.7$, angle $\alpha = 30$ deg, and length $L/D = 4.7$. Adiabatic effectiveness experiments were conducted for blowing ratios ranging from $M = 0.5$ to 2 for both high and low density ratios, following the test matrix in Table 4.

Contour plots for the adiabatic effectiveness tests are shown in Fig. 9 for high and low density ratios. High density ratio contours are on the left and low density ratio contours are on the right. The best cooling overall is at high density ratio and $M = 0.6$ ($I = 0.21$, $VR = 0.36$). The contours show increased spreading and an attached jet in the high density ratio $M = 0.6$ case compared to higher momentum flux ratios. At high density ratio, the jet starts to detach as the blowing ratio and momentum flux ratio increase. At $M = 1$ ($I = 0.64$, $VR = 0.63$), the jet necks as it exits the film-cooling hole with a reduction in cooling effectiveness. At the blowing ratio $M = 2$ at high density ratio ($I = 2.4$, $VR = 1.2$), as shown in Fig. 9(c), the jet detaches almost completely and the surface sees little cooling.

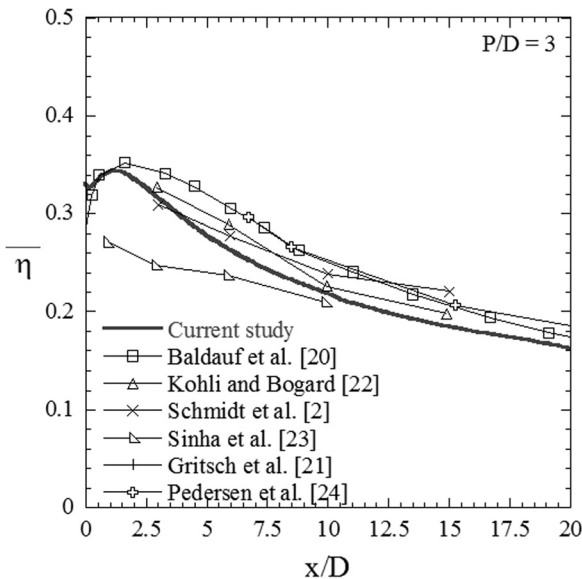


Fig. 8 Laterally averaged film-cooling effectiveness at high density ratio at $M = 0.5$

Table 4 Experimental test conditions for $P/D = 6.7$

M	DR	I	VR	Adiabatic effectiveness	TRDPIV P1	TRDPIV P2
0.6	1.6	0.23	0.38	✓	✓	✓
0.6	1.2	0.3	0.5	✓	✓	✓
1	1.6	0.63	0.63	✓	✓	✓
1	1.2	0.83	0.83	✓	✓	✓
2	1.6	2.5	1.3	✓	✓	✓
2	1.2	3.3	1.7	✓	✓	✓

At low density ratio, similar phenomena occur. At $M = 0.5$ ($I = 0.22$, $VR = 0.42$), the effectiveness is highest and decreases with increasing blowing ratio. Necking occurs as blowing ratio increases to $M = 1$ ($I = 0.87$, $VR = 0.84$), with low density ratio showing more blowoff than high density ratio. In addition, the high density ratio test for a given blowing ratio provides an improved lateral spreading over the corresponding low density ratio test. This increased spreading leads to better film-cooling effectiveness. Schmidt et al. [2] and Wayne and Bogard [3] similarly found an increase in effectiveness at high density ratio over low density ratio.

Adiabatic effectiveness plotted along the centerline is shown in Fig. 10. For both density ratios, the $M = 0.6$ case shows the best cooling. As indicated by the decrease at $x/D = 1$ and subsequent increase at $x/D = 3$, the jet detaches and then reattaches at $M = 1$ at both high and low density ratios. At $M = 2$ for high density ratio, the centerline effectiveness drops off almost immediately and remains largely constant, indicating that the jet does not reattach but instead is fully detached.

The widely-spaced cylindrical hole study was validated against literature studies for laterally averaged results. Comparable studies were done by Schmidt et al. [2] and Wayne and Bogard [3] at wide lateral spacing. Figure 11 shows the laterally averaged results of high density ratio studies at two different blowing ratios compared to the current study. Both studies combined with the current study show agreement between similar parameters at a widely-spaced geometry.

7 Time-Averaged Flowfield Results

The advantage to TRDPIV over other flowfield measurement techniques such as LDV and hot-wire anemometry is the ability to

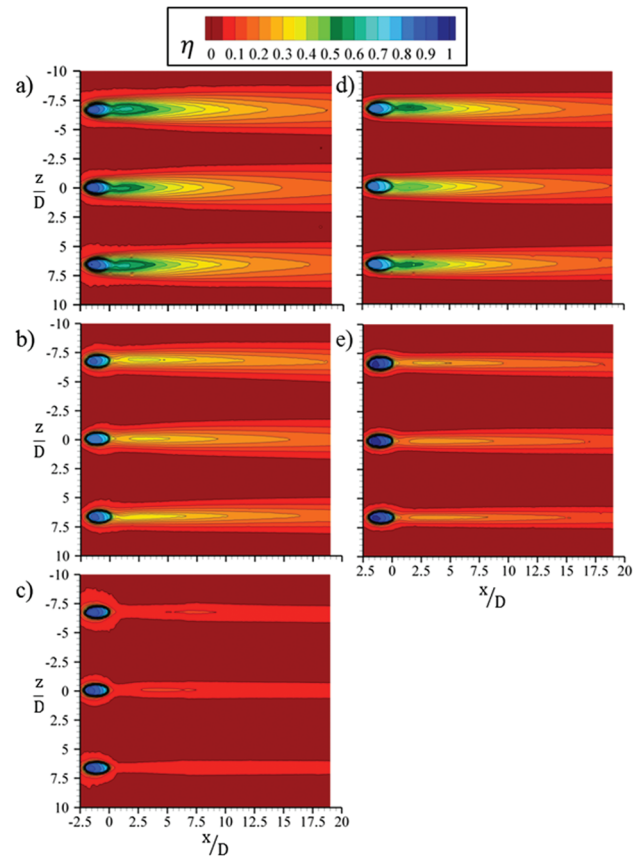


Fig. 9 High (a) and low (b) density ratio effectiveness contours for widely-spaced axial cylindrical holes at blowing ratios (a) $M = 0.6$, $DR = 1.6$ ($I = 0.21$, $VR = 0.36$); (b) $M = 1$, $DR = 1.6$ ($I = 0.64$, $VR = 0.63$); (c) $M = 2$, $DR = 1.6$ ($I = 2.4$, $VR = 1.2$); (d) $M = 0.5$, $DR = 1.2$ ($I = 0.22$, $VR = 0.42$) and (e) $M = 1$, $DR = 1.2$ ($I = 0.87$, $VR = 0.84$)

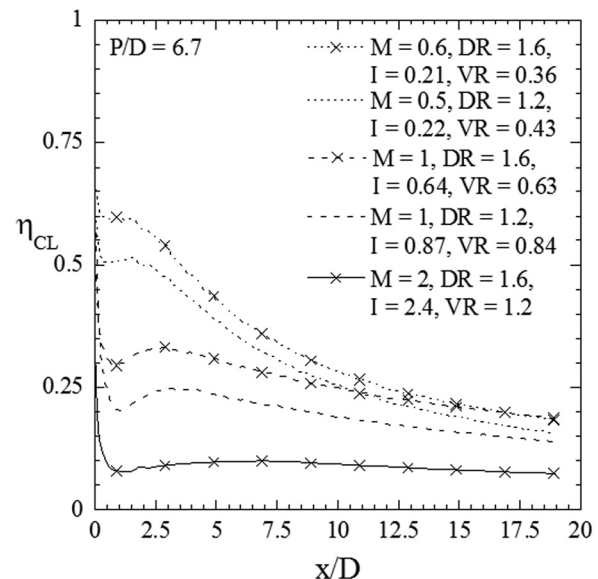


Fig. 10 Centerline film-cooling effectiveness with respect to downstream distance

capture an entire two-dimensional spatial map at an instant in time. The following section presents the time-averaged results of the film-cooling flowfield experiments. Flowfield measurements were taken in two planes parallel to the streamwise direction of

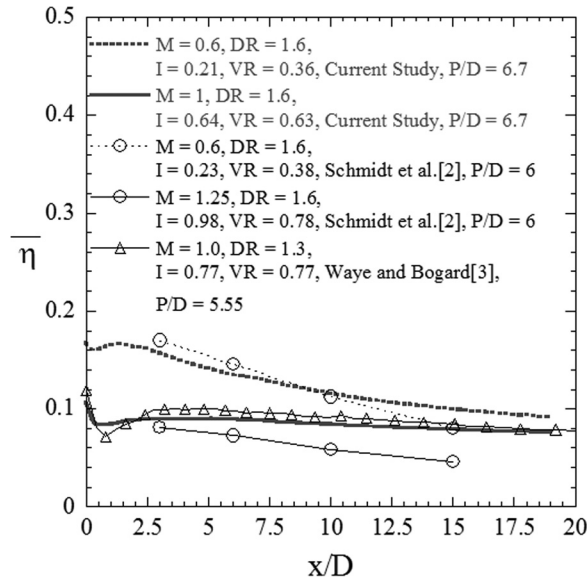


Fig. 11 Laterally averaged film-cooling effectiveness at high density ratio with respect to downstream distance, compared to Schmidt et al. [2] and Waye and Bogard [3]

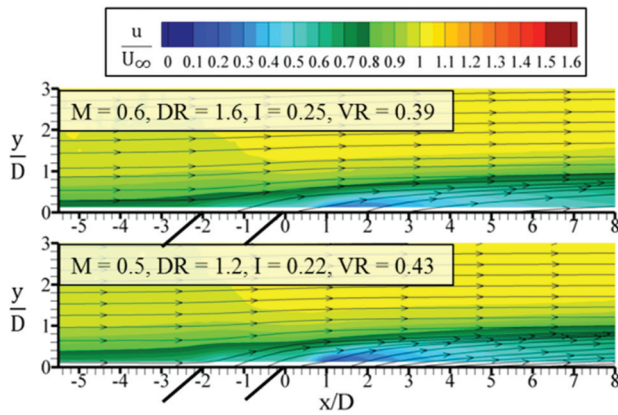


Fig. 12 Time-averaged streamwise velocity contours and streamlines for high and low density ratio at P1 and low momentum flux ratio

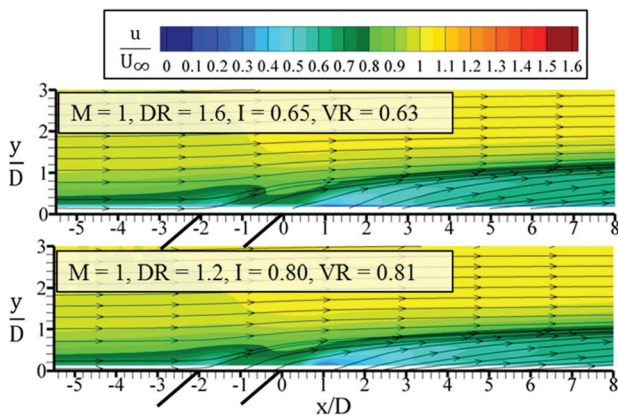


Fig. 13 Time-averaged streamwise velocity contours and streamlines for high and low density ratio at P1 and $M = 1$

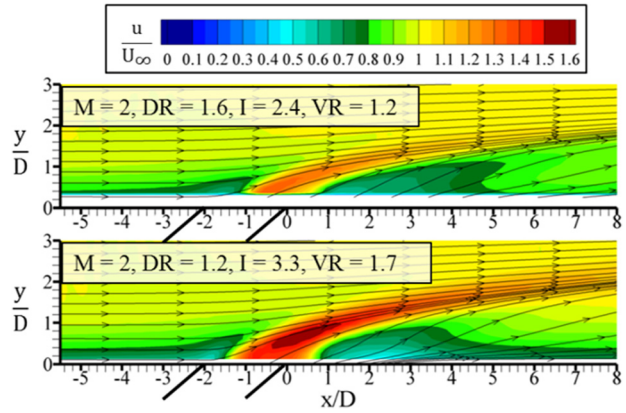


Fig. 14 Time-averaged streamwise velocity contours and streamlines for high and low density ratio at P1 and $M = 2$

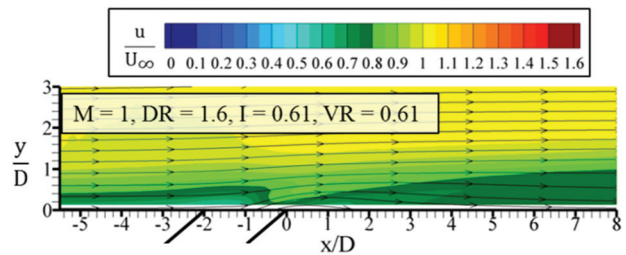


Fig. 15 Time-averaged streamwise velocity contours and streamlines for high density ratio at P2 and $M = 1$

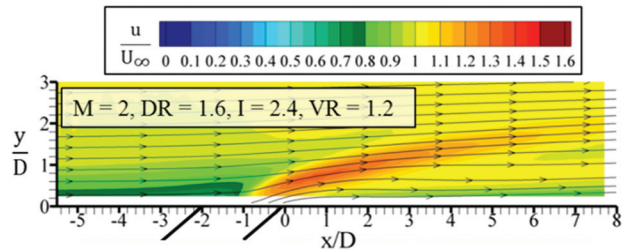


Fig. 16 Time-averaged streamwise velocity contours and streamlines for high density ratio at P2 and $M = 2$

flow (P1 and P2) as was shown in Fig. 2. Experiments were conducted to follow the test matrix listed in Table 4.

Contours for streamwise velocity at the hole center plane (P1) are given in Figs. 12–14 for three different blowing ratios at both low and high density ratios. At $M = 0.6$ for both high and low density ratios as shown in Fig. 12, the similarity in the streamwise velocity contours can be attributed to the similarity in momentum flux ratio of $I = 0.22$ at low density ratio and $I = 0.25$ at high density ratio. The streamlines for both high and low density ratios at $M = 0.6$ are parallel to the wall, indicating little flow detachment in both cases.

The $M = 1$ cases at high density ratio ($I = 0.65, VR = 0.63$) and low density ratio ($I = 0.80, VR = 0.81$) are shown in Fig. 13. A noticeable area of flow blockage just upstream of the film-cooling hole exists for this case causing the flow upstream of injection to decelerate. The streamlines for both density ratios show a higher penetration than the low blowing ratio.

The $M = 2$ test cases for high density ratio ($I = 2.4, VR = 1.2$) and low density ratio ($I = 3.3, VR = 1.7$) are shown in Fig. 14.

···×··· M = 0.6, DR = 1.6, I = 0.25, VR = 0.39
 ···○··· M = 0.5, DR = 1.2, I = 0.22, VR = 0.43
 ·-×-· M = 1, DR = 1.6, I = 0.65, VR = 0.63
 ·-○-· M = 1, DR = 1.2, I = 0.80, VR = 0.81
 -×- M = 2, DR = 1.6, I = 2.4, VR = 1.2
 -○- M = 2, DR = 1.2, I = 3.3, VR = 1.7
 ·-□-· M = 1, DR = 1, I = 1, VR = 1

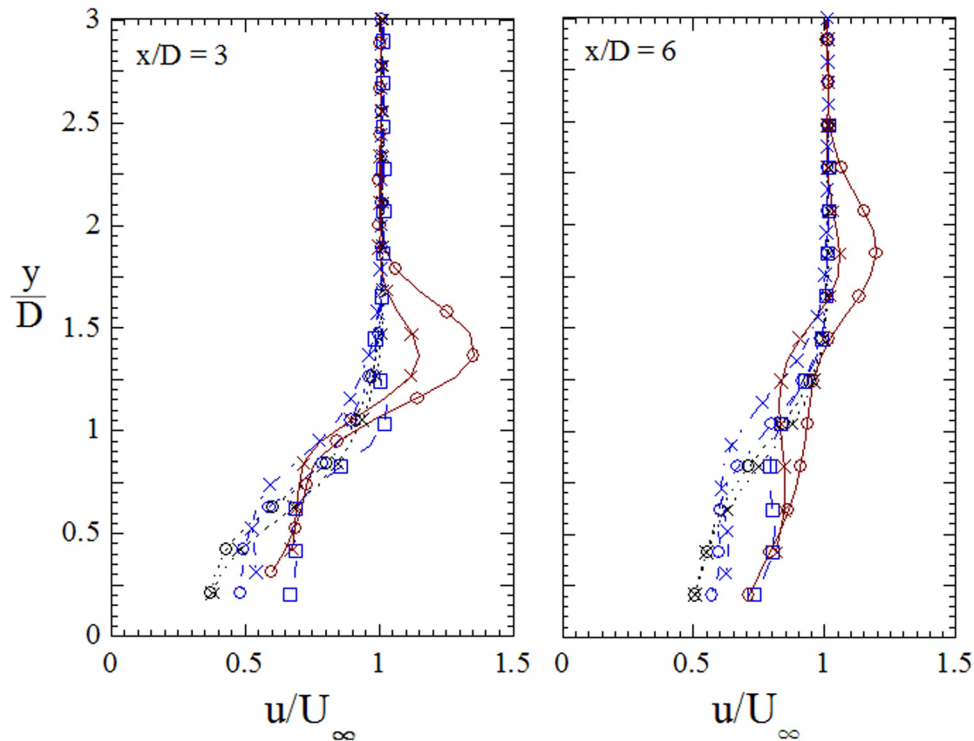


Fig. 17 High and low density ratio streamwise velocity profile at $x/D = 3$ (a) and $x/D = 6$ (b) for P1

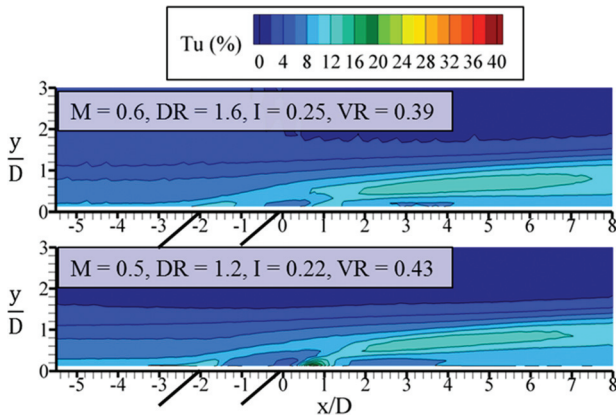


Fig. 18 Turbulence intensity contours at high and low density ratios for $M = 0.6$ and P1

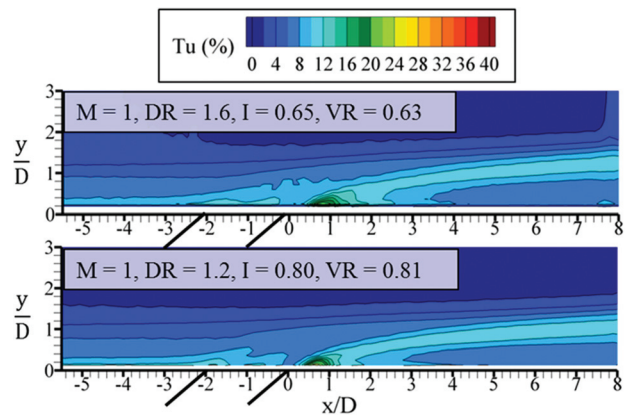


Fig. 19 Turbulence intensity contours at high and low density ratios for $M = 1$ at P1

The maximum velocity in the flowfield is different between low and high density ratios, with the maximum measured velocity being $u/U_\infty = 1.6$ at low density ratio and $u/U_\infty = 1.3$ at high density ratio. As was seen also at $M = 1$, there is a region of low velocity upstream of the film-cooling injection due to jet blockage. The flow blockage region is larger at low density ratio than high density ratio because of the stronger jet momentum at the low density ratio. The streamlines at $M = 2$ follow a trajectory away from the wall (Fig. 14) as compared to lower blowing ratios. The

large flowfield differences for the $M = 2$ can be attributed to the larger difference in momentum flux ratio as compared to the $M = 0.6$ case where the momentum flux is nearly the same between density ratios.

The streamwise velocity contours at the hole edge plane (P2) clearly show effects of the CRVP. At $M = 1$, the measurements show high velocity coolant near the wall (Fig. 15) that is not seen at the hole centerline in P1 (Fig. 13). In this case, the CRVP has mixed the freestream fluid in toward the wall. Figure 16 shows

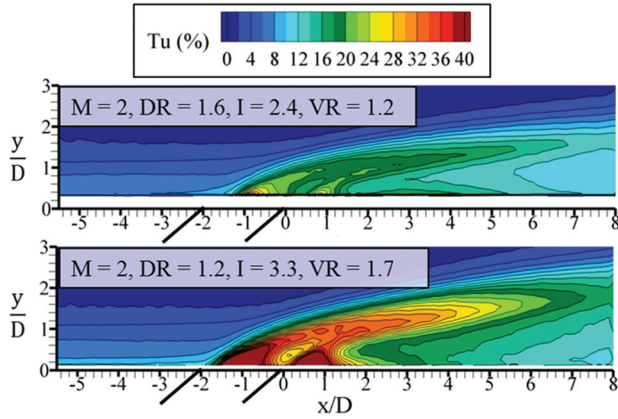


Fig. 20 Turbulence intensity contours at high and low density ratios for $M = 2$ at P1

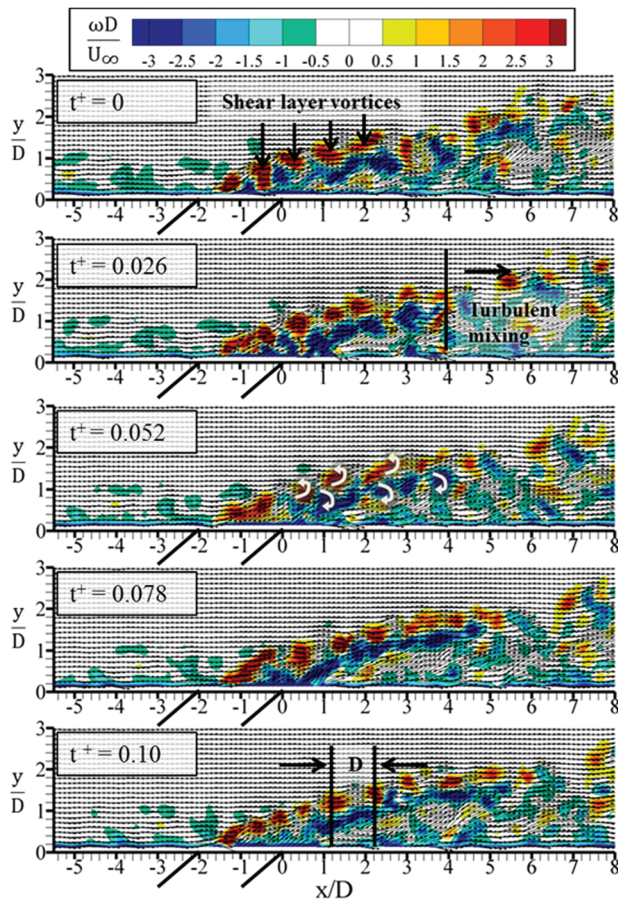


Fig. 21 Time-resolved velocity vectors and vorticity contours at $DR = 1.2$, $M = 2$ ($I = 3.3$, $VR = 1.7$) at P1

spreading in the vertical direction at $M = 2$, again with higher velocity fluid closer to the wall at P2 than at P1 (Fig. 14). This spreading behavior points to the effect of the CRVP, which pushes high-velocity fluid away from the wall at the hole centerline, but toward the wall at the hole edge. The streamlines travel primarily in the positive vertical direction at the hole centerline but turn back toward the wall at the hole edge. This change in streamline direction indicates that the momentum of the fluid in the streamwise direction is influenced by the effect of the CRVP, and the flow is pushed downward at its lateral edges.

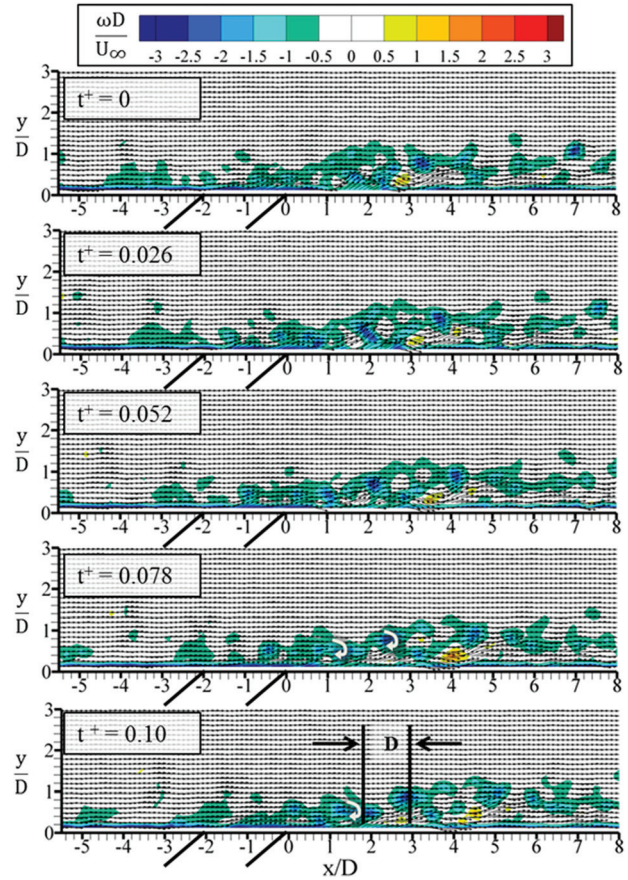


Fig. 22 Time-resolved velocity vectors and vorticity contours for $M = 0.5$, $DR = 1.2$ ($I = 0.22$, $VR = 0.43$) at P1

Streamwise velocity profiles taken at $x/D = 3$ (a) and $x/D = 6$ (b) for the hole center location at high and low density ratios are given in Fig. 17. Only $M = 2$ for both density ratios shows a distinct peak at $x/D = 3$ and 6 with that peak occurring at the same height for both density ratios. Figure 17 indicates the velocity profiles for the $M = 0.6$ blowing ratios are similar to that of a boundary layer. At $x/D = 3$, the near-wall velocity profiles give insight into jet detachment. In the near-wall region for the $M = 1$ and $M = 2$ cases, the velocity profile is nearly constant with a low velocity near the wall indicating circulation and jet detachment. The only case without this low velocity near the wall is the $M = 0.6$ case, which indicates that this is the only jet that does not detach from the surface with this hole geometry. The cases with jet detachment have momentum flux ratios higher than $I = 0.6$ and velocity ratios higher than $VR = 0.6$. There is closer scaling between density ratios at $x/D = 6$, indicating that the cooling jets gradually mix out.

Turbulence intensity contours are shown in Figs. 18–20. Turbulence can be separated into two parts: turbulence exiting the hole and turbulence in the shear layer between the jet and freestream. For all cases, there is elevated turbulence just downstream of injection due to elevated turbulence exiting the hole. The $M = 0.6$ blowing ratios shown in Fig. 18 indicate nearly similar turbulence levels exiting the hole for low and high density ratio cases. At $M = 1$ as given in Fig. 19, the high turbulent region just downstream of the injection appears to have higher turbulence than in the low blowing ratio case due to the jet detachment. Very high turbulence levels exist in the exiting cooling jet and in the shear region for the highest blowing ratio at $M = 2$. These high turbulence levels exiting the hole merge with those found in the separated region and convect far downstream of the hole.

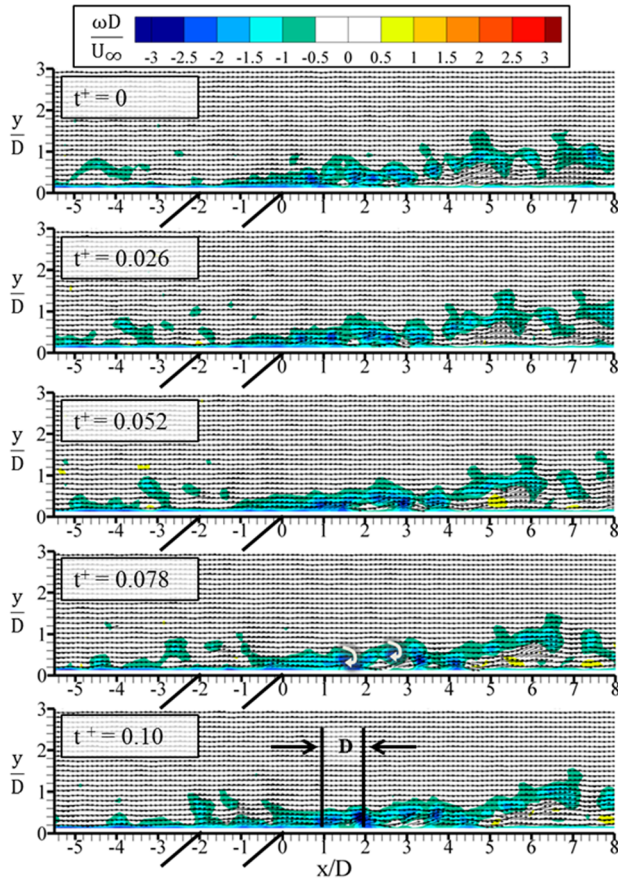


Fig. 23 Time-resolved velocity vectors and vorticity contours for $M = 0.6$, $DR = 1.6$ ($I = 0.25$, $VR = 0.39$) at P1

The highest turbulence levels were measured at the highest momentum flux condition. At $M = 2$ the high turbulence exiting the hole is attributed to a large separation region inside the hole as the coolant enters the hole. In-hole flowfield measurements taken by Issakhanian et al. [25] have also noted the existence of a separation region at the hole entrance for an inclined hole. The high momentum jets are pushed toward the upstream side of the hole as a result of the separation on the downstream part of the hole entrance. The high momentum jets strongly interact with the freestream forming a high turbulence level over the hole.

Unlike the turbulence intensity of the exiting jet, the turbulence levels in the shear layer do not scale with momentum flux ratio. The lowest shear layer peak turbulence is seen in the $M = 1$ cases, because the product $\rho_c U_c$ is the same as the freestream $\rho_\infty U_\infty$, which creates less turbulent mixing when the two flows interact. Increased turbulence happens when the mass flux between the two flows differs. For this reason, the lower blowing ratio cases have higher peak turbulence in the shear layer than the $M = 1$ cases.

8 Time-Resolved Flowfield Results

Time-resolved PIV data were obtained to gather an understanding of the time-dependent nature of the flowfield. Figures 21–23 show instantaneous velocity vectors overlaid on a contour plot of instantaneous vorticity at P1. The time-resolved images shown are successive and the time step between each image is $\Delta t^+ = 0.026$.

At $M = 2$ and low density ratio ($I = 3.3$, $VR = 1.7$) shown in Fig. 21, the vorticity is positive (counterclockwise) emanating from the upstream edge of the hole and the vorticity is negative (clockwise) coming from the downstream edge of the hole. The vorticity contours in the time-resolved flowfield appear as small vortical instabilities that convect downstream with the flow. Close to the hole, the vortical instabilities are spaced approximately one

hole diameter apart. As the flow convects further downstream starting at approximately $x/D = 4$, the vorticity breaks down into random turbulence.

This vorticity is the result of the shear layer between the jet and the freestream flow. The vortical structures take the appearance of Kelvin–Helmholtz style instabilities close to the injection before becoming completely turbulent. Similarly, Fawcett et al. [10] observed Kelvin–Helmholtz type breakdown of the shear layer using flow visualization at a similar blowing ratio for cylindrical holes.

Instantaneous velocity vectors for $M = 0.5$, $DR = 1.2$ ($I = 0.25$, $VR = 0.39$) at the centerline plane overlaid onto vorticity contours are shown in Fig. 22. Instead of two distinct regions of positive and negative vorticity, only negative vorticity is seen in this flow. In this $M = 0.5$, $DR = 1.2$ flow, there are similarly small vortical instabilities with a length scale of approximately one diameter just downstream of the hole exit. The main difference between $M = 2$ and $M = 0.5$ flows is the strength of the vorticity and the direction of the shear layer roll-up.

At the same momentum flux ratio but at a high density ratio, the time-resolved data in Fig. 23 shows the same vortical structures as in Fig. 22. At high density ratio and matched momentum flux ratio, however, the vortical structures are closer to the wall than at low density ratio for streamwise locations close to the hole. These results indicate the importance of density ratio as a scaling parameter.

9 Conclusions

A new facility was constructed and benchmarked to conduct film-cooling studies at low and high density ratios. The first set of high density ratio data from this facility compares well to previous high density ratio studies. The facility can accommodate both flowfield and adiabatic effectiveness experiments.

The adiabatic effectiveness measurements indicated increased spreading for the same mass flux ratio at the high density ratio when the jet remained attached to the surface. As the momentum flux ratio increased, jet separation occurred as expected.

Flowfield measurements indicated a velocity deficit occurred for $M = 1$ and 2 at high and low density ratios, indicating that $M = 0.6$ was the only case with jets that were attached to the wall. The counter-rotating vortex pair had an effect on the velocity of the flow near the wall at the hole edge, bringing in high velocity fluid from the freestream close to the wall.

The turbulence levels of the exiting jet were found to scale with the momentum flux ratio of the jet, with the lowest momentum flux ratio jet exhibiting the minimum turbulence intensity. In the shear layer, the minimum turbulence intensity was for a unity blowing ratio because of the matched mass flux ratio between the jet and the freestream.

Time-resolved flowfield measurements showed the behavior of the shear layer vortices, which took the form of shear layer roll-up. The size and spacing of the shear layer vortices were relatively consistent between momentum flux ratio cases.

In addition to providing time-averaged and time-resolved data for a film-cooling flow for a widely-spaced cylindrical geometry, this set of data can be used to compare to computational work at high and low density ratios.

Acknowledgment

We gratefully acknowledge United Technologies—Pratt & Whitney for their support on this project. We would also like to thank Robert Schroeder for his assistance in building the test facility and Chris Whitfield for his assistance in gathering the data.

Nomenclature

- C_f = skin friction coefficient, $0.0456/Re_\delta^{1/4}$
 D = diameter of film-cooling holes

DR = density ratio, ρ_c/ρ_∞
 I = momentum flux ratio, $\rho_c U_c^2/\rho_\infty U_\infty^2$
 L = injection hole length
 M = blowing ratio, $\rho_c U_c/\rho_\infty U_\infty$
 P = lateral distance between holes, pitch
 px = one measurement pixel
 Re = jet Reynold's number, $U_j D/\nu$
 Re_δ = boundary layer Reynold's number, $U_\infty \delta/\nu$
 t = time
 T = temperature
 Tu(%) = turbulence intensity percentage, $\sqrt{0.5(u_{rms}^2 + v_{rms}^2)}/U_\infty$
 U = x-velocity
 u^* = friction velocity, $U_\infty \sqrt{c_f/2}$
 V = y-velocity
 VR = velocity ratio, U_c/U_∞
 x = streamwise distance measured from the hole downstream edge
 y = vertical distance measured from the wall surface
 z = lateral distance measured from the center axis of the center hole
 Δt^+ = time nondimensionalized by friction velocity, tu^*/δ

Greek Symbols

α = injection angle
 δ = 99% boundary layer thickness
 η = local adiabatic effectiveness, $(T_\infty - T_{aw})/(T_\infty - T_c)$
 θ = momentum thickness
 ρ = fluid density
 ν = kinematic viscosity

Superscripts

$'$ = fluctuating/rms value
 $-$ = average value
 $+$ = nondimensionalized by wall variables
 \sim = instantaneous value
 $*$ = friction value, nondimensionalized by u^*

Subscripts

aw = adiabatic wall
 c = coolant
 CL = centerline
 j = jet
 w = wall
 ∞ = freestream

References

- [1] Pietrzyk, J.R., Bogard, D.G., and Crawford, M.E., 1989, "Hydrodynamic Measurements of Jets in Crossflow for Gas Turbine Film Cooling Applications," *ASME J. Turbomach.*, **111**(2), pp. 139–145.
- [2] Schmidt, D. L., Sen, B., and Bogard, D. G., 1996, "Film Cooling With Compound Angle Holes: Adiabatic Effectiveness," *ASME J. Turbomach.*, **118**(4), pp. 807–813.
- [3] Waye, S. K., and Bogard, D. G., 2006, "High Resolution Film Cooling Effectiveness Comparison of Axial and Compound Angle Holes on the Suction Side of a Turbine Vane," *ASME Paper No. GT2006-90225*.
- [4] Pietrzyk, J. R., Bogard, D. G., and Crawford, M. E., 1990, "Effects of Density Ratio on the Hydrodynamics of Film Cooling," *ASME J. Turbomach.*, **112**(3), pp. 437–443.
- [5] Fric, T. F., and Roshko, A., 1994, "Vortical Structure in the Wake of a Transverse Jet," *J. Fluid Mech.*, **279**, pp. 1–47.
- [6] Haven, B. A., and Kurosaka, M., 1997, "Kidney and Anti-Kidney Vortices in Crossflow Jets," *J. Fluid Mech.*, **352**, pp. 27–64.
- [7] Auf dem Kampe, T., Völker, S., Sämel, T., Heneka, C., Ladisch, H., Schulz, A., and Bauer H.-J., 2011, "Experimental and Numerical Investigation of Flow Field and Downstream Surface Temperatures of Cylindrical and Diffuser Shaped Film Cooling Holes," *ASME Paper No. GT2011-45106*.
- [8] Bernsdorf, S., Rose, M. G., and Abhari, R. S., "Modeling of Film Cooling—Part I: Experimental Study of Flow Structure," *ASME J. Turbomach.*, **128**(1), pp. 141–149.
- [9] Tanahashi, M., Hirayama, T., Taka, S., and Miyauchi, T., 2008, "Measurement of Fine Scale Structure in Turbulence by Time-Resolved Dual-Plane Stereoscopic PIV," *Int. J. Heat Fluid Flow*, **29**(3), pp. 792–802.
- [10] Fawcett, R. J., Wheeler, A. P. S., He, L., and Taylor, R., 2012, "Experimental Investigation Into Unsteady Effects on Film Cooling," *ASME J. Turbomach.*, **134**(2), p. 021015.
- [11] Polanka, M.D., 1999, "Detailed Film Cooling Effectiveness and Three Component Velocity Field Measurements on a First Stage Turbine Vane Subject to High Freestream Turbulence," Ph.D. thesis, The University of Texas at Austin, Austin, TX.
- [12] Eberly, M., 2012, "Time-Resolved Studies of High Density Ratio Film-Cooling Flows," M.S. thesis, The Pennsylvania State University, State College, PA.
- [13] LaVision, 2013, "LaVision—We Count on Photons," LaVision, Goettingen, Germany, accessed September 23, 2012, <http://www.lavision.de/en/>
- [14] Figliola, R. S., and Beasley, D. E., 2006, *Theory and Design for Mechanical Measurements*, Wiley, New York.
- [15] Moffat, R. J., 1988, "Describing the Uncertainties in Experimental Results," *Exp. Therm. Fluid Sci.*, **1**(1), pp. 3–17.
- [16] Raffel, M., Willert, C. E., and Kompenhans, J., 1998, *Particle Image Velocimetry: A Practical Guide*, Springer, New York.
- [17] Scarano, F., and Riethmuller, M. L., 2000, "Advances in Iterative Multigrid PIV Image Processing," *Exp. Fluids*, **29**(0), pp. S051–S060.
- [18] Harder, K. J., and Tiederman, W. G., 1991, "Drag Reduction and Turbulent Structure in Two-Dimensional Channel Flows," *Philos. Trans. R. Soc. London, Ser. A*, **336**(1640), pp. 19–34.
- [19] Thole, K., Gritsch, M., Schulz, A., and Wittig, S., 1998, "Flowfield Measurements for Film-Cooling Holes With Expanded Exits," *ASME J. Turbomach.*, **120**(2), pp. 327–336.
- [20] Baldauf, S. Scheurlen, M. Schulz, A. and Wittig S., 2002, "Correlation of Film-Cooling Effectiveness From Thermographic Measurements at Engine Like Conditions," *ASME J. Turbomach.*, **124**(4), pp. 686–698.
- [21] Gritsch, M. Schulz, A. and Wittig S., 1998, "Adiabatic Wall Effectiveness Measurements of Film-Cooling Holes With Expanded Exits," *ASME J. Turbomach.*, **120**(3), p. 549.
- [22] Kohli, A., and Bogard D. G., 1997, "Adiabatic Effectiveness, Thermal Fields, and Velocity Fields for Film Cooling With Large Angle Injection," *ASME J. Turbomach.*, **119**(2), p. 352.
- [23] Sinha, A. K., Bogard, D. G., and Crawford M. E., 1991, "Film-Cooling Effectiveness Downstream of a Single Row of Holes With Variable Density Ratio," *ASME J. Turbomach.*, **113**(3), p. 442.
- [24] Pedersen, D. R., Eckert, E. R. G., and Goldstein R. J., 1977, "Film Cooling With Large Density Differences Between the Mainstream and the Secondary Fluid Measured by the Heat-Mass Transfer Analogy," *ASME J. Heat Transfer*, **99**, pp. 620–627.
- [25] Issakhanian, E., Elkins, C. J., and Eaton, J. K., 2012, "In-Hole and Mainflow Velocity Measurements of Low-Momentum Jets in Crossflow Emanating From Short Holes," *Exp. Fluids*, **53**(6), pp. 1765–1778.